RSC Advances

PAPER

View Article Online
View Journal | View Issue

Cite this: *RSC Adv.*, 2016, **6**, 82984

Facile, ethylene glycol-promoted microwave-assisted solvothermal synthesis of high-performance $LiCoPO_4$ as a high-voltage cathode material for lithium-ion batteries†

Jennifer Ludwig,[a] Cyril Marino,‡[b] Dominik Haering,[b] Christoph Stinner,[c] Dennis Nordlund,[d] Marca M. Doeff,[e] Hubert A. Gasteiger[b] and Tom Nilges*[a]

Received 4th August 2016
Accepted 23rd August 2016

DOI: 10.1039/c6ra19767a

www.rsc.org/advances

Olivine-type $LiCoPO_4$ is considered a promising high-voltage cathode material for next-generation lithium-ion batteries. However, preparing high-performance $LiCoPO_4$ by a simple approach has been challenging. Herein, we present a facile and rapid (30 min) one-step microwave-assisted solvothermal synthesis route using a 1 : 1 (v/v) water/ethylene glycol (EG) binary solvent mixture and a temperature of 250 °C. The technique delivers high-performance $LiCoPO_4$ nanoparticles without additional post-annealing or carbon coating steps. The as-prepared powder consists of single crystalline $LiCoPO_4$ and features a hexagonal platelet-like morphology with dimensions of 700–800 nm × 400–600 nm × 100–220 nm. Selected area electron diffraction (SAED) experiments reveal that the platelets show the smallest dimension along [010], which is the direction of the lithium diffusion pathways in the olivine crystal structure. Furthermore, the results indicate that the EG co-solvent plays an important role in tailoring the particle size, morphology, and crystal orientation of the material. Co L-edge soft X-ray absorption spectroscopy (XAS) of $LiCoPO_4$ are presented for the first time and confirm that the material only consists of Co^{2+}. Benefiting from the unique morphology, which facilitates Li-ion conduction, electrochemical measurements deliver an initial discharge capacity of 137 mA h g^{-1} at 0.1 C, a remarkably stable capacity retention of 68% after 100 cycles at 0.5 C, and a specific energy density of 658 W h kg^{-1} based on its capacity and voltage, which is the best performance of $LiCoPO_4$ obtained from microwave-assisted solvothermal synthesis to date.

Introduction

The scientific community predicts that effects on climate change due to the burning of fossil fuels will be significant within the next twenty years. Global warming is an important challenge for mankind and solutions need to be found. The development of electric vehicles powered by fuel cells or lithium-ion batteries can play a key role in reducing CO_2 gas emissions, which is considered to be a main cause of the greenhouse effect. For the past 30 years, scientists have been looking for the perfect combination of electrolyte, an anode material, and a cathode material for building the best Li-ion battery with high energy density, good cycling and acceptable safety characteristics. Since their introduction by Padhi *et al.*,[1] olivine-structured lithium transition-metal orthophosphates with the formula $LiMPO_4$ (M = Fe, Mn, Co, Ni) have attracted considerable attention as cathode materials for lithium-ion batteries due to their high specific capacities and thermal stability.[2–7] Within the phospho-olivine family, $LiFePO_4$ (LFP) has widely been investigated and is a fully developed material that is nowadays available for commercial applications.[8] The

[a]*Technical University of Munich, Department of Chemistry, Synthesis and Characterization of Innovative Materials, Lichtenbergstr. 4, 85747 Garching, Germany. E-mail: tom.nilges@lrz.tu-muenchen.de*

[b]*Technical University of Munich, Department of Chemistry, Technical Electrochemistry, Lichtenbergstr. 4, 85747 Garching, Germany*

[c]*BMW AG, Petuelring 130, 80788 München, Germany*

[d]*Stanford Synchrotron Radiation Lightsource, SLAC National Accelerator Laboratory, 2575 Sand Hill Rd, Menlo Park, CA, 94025, USA*

[e]*Lawrence Berkeley National Laboratory, Environmental Energy Technologies Division, 1 Cyclotron Rd, Berkeley, CA, 94720, USA*

† Electronic supplementary information (ESI) available: State of the art of HT, ST, SCF, MWHT, and MWST synthesis of LCP; PXRD measurement of an empty capillary; PXRD of $Li_2SO_4 \cdot H_2O$ obtained from the reaction solution; Rietveld fit of LCP-MW-w; cell parameters, atomic coordinates, thermal displacement parameters, and selected interatomic distances obtained from all Rietveld refinements; TGA/DSC and temperature-dependent *in situ* PXRD data of LCP-MW; FTIR and Raman spectra; additional SEM images; additional electrochemical measurements of LCP-MW materials with varying amounts of Li_2SO_4 and of electrodes with high loading. CCDC 1500138–1500140. For ESI and crystallographic data in CIF or other electronic format see DOI: 10.1039/c6ra19767a

‡ Present address: Paul Scherrer Institute, Electrochemical Energy Storage, 5232 Villigen PSI, Switzerland.

use of iron-based cathodes for lithium-ion batteries has several advantages, including abundant and cheap raw materials, high thermal stability and relatively low toxicity.[5,9,10] Moreover, with a theoretical capacity of 170 mA h g^{-1}, LFP operates at a voltage of 3.45 V *versus* Li/Li^+,[1] which is compatible with commercially available electrolytes used in current lithium-ion battery technology. However, in recent years the scientific community has increasingly been focusing on the isostructural $LiMnPO_4$ (LMP), $LiCoPO_4$ (LCP) and $LiNiPO_4$ (LNP) type phospho-olivines due to the possibility of increasing the specific energy with these compounds.[7,11–13] The Mn^{2+}/Mn^{3+}, Co^{2+}/Co^{3+}, and Ni^{2+}/Ni^{3+} redox couples have been shown to operate at much higher voltages of 4.1 V,[1] 4.8 V,[14] and 5.1 V,[15] respectively, and are thus paving the way for next generation high-energy-density olivine-based Li-ion batteries.[3]

The redox potential of LNP is too high for use with common electrolytes and the electrochemical activation of the compound remains a challenge.[3,15,16] The high-voltage cathode material LCP with a lower operating voltage features the highest energy of 802 W h kg^{-1} within the olivine family and a theoretical capacity of 167 mA h g^{-1}.[14] However, the low electronic[17,18] and ionic[19] conductivities of LCP as well as the limited oxidative stability of standard electrolytes[20,21] remain major obstacles to successful utilization. All these disadvantages result in an unsatisfactory electrochemical performance of LCP, including low practical capacities, poor rate performance, and short cycle life.[3]

Tremendous efforts have been made in recent years to mitigate these limitations. In particular, chemical doping,[17,22,23] carbon coating,[24,25] and particle size reduction[26–29] have been extensively used to improve the electrochemical activity of LCP. The importance of nanostructural engineering to the electrochemical performance has also been examined for other types of cathode materials, such as spinel-type transition metal oxides.[30] Theoretical studies suggest that despite the fact that Li^+ ions are located in one-dimensional channels along [010] and [001] in the olivine crystal structure (Fig. 1b and c), lithium diffusion is only promoted along the [010] pathway (Fig. 1b).[22,31,32] Thus, reducing the particle dimensions along the *b* direction can result in faster Li-ion diffusion and improved electrochemical properties as shown recently by Rui and co-workers.[29] After 50 cycles at 0.2 C, a discharge capacity of 136 mA h g^{-1} for $LiCoPO_4$/C nanosheets was reported compared to only 54 mA h g^{-1} for bulk particles, which is the best performance reported for carbon-coated LCP to date. Nanosheets exhibit a large surface-to-volume ratio that allows a more effective electrode–electrolyte contact area. Nevertheless, the multi-step preparation, which requires solid-state synthesis of a $NH_4CoPO_4 \cdot H_2O$ precursor, followed by a liquid-phase exfoliation and a high-pressure high-temperature lithiation by a supercritical fluid (SFC) process in ethanol precludes easy scale-up and industrial applicability. A simpler and faster synthetic approach towards high-performance LCP with small dimensions along [010] and the option for large-scale production is yet to be fully developed, to the best of our knowledge.

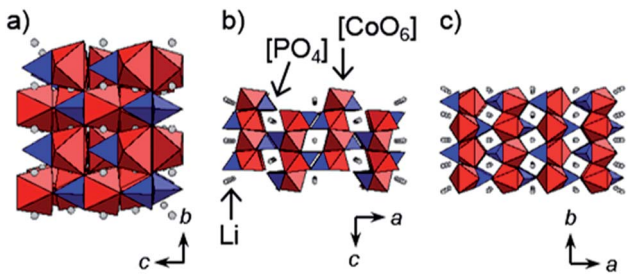

Fig. 1 Projections of the crystal structures of olivine-type $LiCoPO_4$ (space group *Pnma*) along the three crystallographic axes: (a) [100], (b) [010], and (c) [001]. $[CoO_6]$ octahedra are drawn in red, $[PO_4]$ tetrahedra in blue, and Li ions in grey.

With regard to the synthetic method, conventional solid-state reactions have been the dominant technique.[33–35] The process, however, generally requires high temperatures and an additional ball milling step, making this approach unfeasible for potential industrial applications. Hydrothermal (HT)[36–40] or solvothermal (ST)[29,41–44] approaches are of greater interest due to the facile and easily scalable process, mild reaction conditions, and the possibility of preparing nanomaterials with controllable and uniform particle sizes, shapes and crystal orientations.[45] From a practical point of view, however, the conventional HT or ST approach can be limited by slow reaction kinetics and non-uniform reaction conditions due to thermal gradients that are caused by the convective heating. This results in heterogeneous particle size distributions and morphologies and hence, inferior electrochemical performance.[46] Only a few reports of conventional hydro- or solvothermal products indicate a direct formation of crystalline LCP materials without high-temperature annealing in a single step.[36–38,44] Furthermore, the materials often show antisite defects and disordered structures and therefore require additional thermal treatments at very high temperatures (~800–900 °C), or additional carbon coating steps to obtain reasonable electrochemical performances.[37,39,42] The microwave-assisted (MW) approach, which is quite new in the research field of LCP,[47–51] is particularly appealing because of the direct dielectric heating by the use of microwave irradiation, which allows short reaction times of only several minutes and more uniform reaction conditions due to lower thermal gradients in the reaction vessel.[46,48,52] The method allows uniform nucleation and produces highly crystalline materials with homogeneous particle size distributions and morphologies.[48,52] The electrochemical performance of LCP obtained by MWST synthesis without post-calcination steps is comparable to ST materials that have been annealed at high temperature. A detailed overview of the state of the art in the hydrothermal and solvothermal synthesis of LCP, including supercritical fluid and microwave-assisted techniques is given in Table S1 (ESI).†

Very recently, combining an organic solvent and water in a mixed system has become popular in the solvothermal synthesis of $LiCoPO_4$ nanocrystals.[42,44,53] The solvent blend is supposed to be beneficial for effectively regulating the morphology and crystal orientation due to the soft template effect of the organic solvent,[42,54] and also promotes the complete dissolution of the reagents with the help of the water

component. However, the effect of crystallographic orientation and particle morphology on the electrochemical performance of LCP has barely been touched upon.[29,41,48,55]

Herein, a novel, simple and fast microwave-assisted solvothermal (MWST) approach towards high-performance LCP at moderate temperatures (250 °C) using ethylene glycol (EG) as a co-solvent is presented for the first time. Unlike other procedures, the innovative technique does not require any post-calcination steps or the use of carbon coatings to improve the electrochemical performance. The as-prepared LCP material is fully characterized by X-ray powder diffraction, elemental analysis, scanning and transmission electron microscopy, Brunauer–Emmett–Teller surface area measurements, infrared and Raman spectroscopy, thermogravimetric measurements as well as electrochemical measurements. Based on these measurements, the relationship between the synthesis, morphology, and electrochemical properties of the material is elucidated. Moreover, Co L-edge soft X-ray absorption spectroscopic data on LCP are presented for the first time.

Experimental

Microwave-assisted solvothermal synthesis

A microwave-assisted solvothermal (MWST) process based on a previous report for $LiMn_{0.7}Fe_{0.3}PO_4$ (ref. 56) was modified with regard to power of the microwave irradiation, synthesis temperature and pH in order to obtain pure olivine-type LCP. 22.5 mmol of $LiOH \cdot H_2O$ (Bernd Kraft, ≥99.0%), 7.5 mmol of $CoSO_4 \cdot 7H_2O$ (Chempur, 99%), and 7.5 mmol of H_3PO_4 (AppliChem, Ph. Eur., 85 wt% solution) were dissolved in 30 mL of a 1 : 1 (v/v) mixed solvent of deionized water (high-purity water type I, Millipore, 18.2 MΩ cm) and ethylene glycol (VWR AnalaR NORMAPUR, 99.9%). The molar ratio of Li : Co : P was 3 : 1 : 1. Note that the two additional moles of Li are necessary to bind the sulfate in the reaction (*cf.* Scheme 1a) and that a 1 : 1 : 1 ratio did not result in the formation of the olivine phase. 0.050 g ascorbic acid (Alfa Aesar, 99+%) was added as a reducing agent to prevent oxidation of Co^{2+} to Co^{3+} in the aqueous solution as well as a buffer to keep a suitable pH value to promote the crystallization of single-phase LCP. The resulting blue-violet mixture (pH 5.5, *cf.* graphical abstract) was stirred vigorously and then transferred into a 75 mL PTFE/TFM vessel (HTV-75, MLS GmbH). The solvothermal reaction was performed at 250 °C for 30 min under continuous stirring using an Ethos One microwave system (MLS GmbH, MR-8 HT high-temperature rotor). The internal temperature was maintained by adjusting the power of the microwave irradiation with the automatic T660 temperature control unit (maximum power: 600 W). After natural cooling, the pH of the solution was 5.0. The violet precipitate was collected by filtration, washed five times with 50 mL distilled water and 50 mL absolute ethanol (VWR AnalaR NORMAPUR, 99.95%) followed by drying in air at 150 °C for 12 h. The sample is denoted LCP-MW.

Structural, physical and chemical characterization

X-ray powder diffraction (XRD) patterns were collected on a Stoe STADI P diffractometer using Mo $K_{\alpha 1}$ radiation (Ge(111) monochromator, $\lambda = 0.70930$ Å) and a Dectris MYTHEN DCS 1K silicon solid-state detector. The samples were ground in a mortar and then sealed in 0.5 mm borosilicate glass capillaries (Hilgenberg, glass type no. 50, wall thickness: 0.01 mm). The data were measured in a 2θ range of 3–70° (PSD step: 0.015°; time/step: 25 s, 3 ranges, measurement time: 12 h). Silicon powder ($a = 5.43088$ Å) was used as an external standard. Rietveld fitting of the powder diffraction data was performed using the Jana2006 software package.[57] The background profile was fitted using a Chebyshev function with 35 coefficients. Peak asymmetry at small scattering angles was corrected by the axial divergence model described by Finger *et al.*[58] using empirically determined starting values for the parameters. Moreover, an absorption correction was applied (estimated packing fraction ~0.6).[59] General atomic positions as well as the isotropic thermal displacement parameters of Co, P, and O were refined. The thermal factors of Li, however, were kept fixed because they cannot be determined by X-ray powder diffraction (*cf.* low atomic scattering factor). Finally, the Berar's correction was applied to obtain more realistic values for the estimated standard uncertainties.[60]

Elemental analysis was performed using atomic absorption spectroscopy (Varian AA280FS sequential device) for the Li, and photometry (Shimadzu UV-160 device) for the Co and P contents, respectively. C, H, N, and S contents were analyzed by combustion analysis using a Hekatech Euro EA CHNSO instrument.

The morphologies of the particles were observed using a high-resolution scanning electron microscope (HR-SEM, JEOL JSM-7500F). The gentle beam (GB) mode (accelerating voltage: 1 kV) was used to reduce charging effects of the material. Energy-dispersive X-ray spectroscopy (EDS) was performed at an acceleration voltage of 15 kV and a probe current of 20 μA using a Noran system S1X (Thermo Electron Corporation, model 6714A01SUS-SN) probe attached to the scanning electron microscope.

Transmission electron microscopy (TEM, JEOL JEM-2010, 160 kV, LaB_6 cathode) and selected area electron diffraction (SAED) were performed using specimens dispersed in ethanol and then dropped onto 200 mesh carbon film. Magnetite was used as a reference material for the SAED studies, and the patterns were analyzed using the CrystalMaker software.[61]

The specific surface area of the powder was measured by N_2 adsorption using the Brunauer–Emmett–Teller (BET) method, where eleven points were measured. The measurement was performed on a Quantachrome Autosorb iQ instrument after degassing at 423 K for 12 h.

Soft X-ray absorption spectroscopy (XAS) measurements on the as-prepared $LiCoPO_4$ material were conducted at beamline 8-2 of Stanford Synchrotron Radiation Lightsource (SSRL) using a 1100 mm^{-1} spherical grating monochromator operated with 40 μm entrance and exit slits, providing ~2.0×10^{10} ph s^{-1} at 0.4 eV resolution in a 1 mm^2 beam spot. Two scans of the Co $L_{2,3}$-edge $\mu(E)$ spectra were acquired under ultrahigh vacuum (10^{-9} Torr) at room temperature in the Auger electron yield (AEY), total electron yield (TEY), and fluorescence yield (FY) modes, respectively.[62] After normalizing the spectra to the beam current, the background contribution was subtracted. The

energies scale was corrected using the values reported by Hiberd and co-workers.[63] Additionally, CoO and Co_3O_4 powders were used as reference samples for Co^{2+} and Co^{3+}. For better comparison and plotting, the intensity of all spectra was further normalized to a maximum intensity of 1.

Electrochemical measurements

The electrochemical performance was evaluated using Swagelok cells. The working electrodes were composed of 80 wt% of the as-prepared LCP powder, 10 wt% carbon (Super C65, Timcal), and 10 wt% polyvinylidene difluoride binder (PVDF, Kynar HSV 900, Arkema). LCP, Super C65 and PVDF were mixed with *N*-methyl-2-pyrrolidone (NMP, Sigma Aldrich) and then homogenized at 2000 rpm for 20 min using a planetary centrifugal vacuum mixer (Thinky). The electrode slurry was spread on aluminum foil (15 μm, MTI corporation) and dried at 55 °C for 3–4 h. Electrodes with diameters of 10 mm and typical loadings of 4–5 mg cm^{-2} were punched out, and pressed two times at 250 MPa for 1 min (KBr press, PerkinElmer). Afterwards, the electrodes were additionally dried for 2 h at 120 °C under vacuum in a Büchi B-585 glass oven. The test cells were assembled in an Ar-filled glove box (MBraun; <0.1 ppm H_2O, <0.1 ppm O_2). The cells were cycled between 3.5 V and 5.2 V in two different procedures: (a) three cycles each at 0.1 C, 0.2 C, 0.5 C, 1 C, and 2 C followed by 20 cycles at 0.5 C; (b) 2 initial cycles at 0.067 C followed by 100 cycles at 0.5 C rate. In both procedures, a constant voltage step at 5.2 V was added with a current limited to 0.05 C. Specific capacities were calculated on the basis of the weight of the as-prepared LCP powders in the electrodes (neglecting the weight of the lithium sulfate side phase, as it accounts for only <5 wt%; *cf.* Table 1); C-rates were calculated based on a theoretical specific capacity of 167 mA h g_{LCP}^{-1}.

Results and discussion

X-ray powder diffraction

Fig. 2 shows the Rietveld fit of the X-ray powder diffraction (XRD) data of the as-prepared sample LCP-MW obtained from the simple microwave-assisted solvothermal (MWST) process. All diffraction peaks can be fitted to the orthorhombic olivine structure model (space group *Pnma*, ICSD database no. 247497 (ref. 64)) with good reliability factors (Table S2, ESI†). The refined lattice parameters are $a = 10.1930(7)$ Å, $b = 5.9188(4)$ Å, and $c = 4.6959(3)$ Å. The refined atomic coordinates, thermal displacements parameters, and selected interatomic distances are given in Tables S3 and S4 (ESI†).

No crystalline impurity phases which are generally reported for products from solution-based routes (*e.g.* the poorly soluble Li_3PO_4)[65] are observed within the detection limit of the method. In contrast to conventional hydro- or solvothermal products, which are prone to antisite defects and disordered structures[37] and therefore often have to undergo thermal treatments at very high temperatures (~800–900 °C) to improve electrochemical activity,[39,42] the microwave technique delivers a highly crystalline $LiCoPO_4$ material within a short reaction time of only 30 min and without any post heat treatment. This is evidenced by the appearance of sharp and narrow diffraction peaks. Moreover, the refinement of the occupancies of the Li and Co sites neither suggested a Li-deficient nor a disordered structure. The Co and Li sites were kept fully occupied and an ordered structure was assumed for the refinement. The refined cell volume of 283.31(3) $Å^3$ is smaller than reported values for hydro-[37,66] and solvothermal[44,48] LCP, indicating fewer antisite defects. The observed background profile can mostly be attributed to the borosilicate capillary used (reference measurement of an empty capillary see Fig. S1, ESI†). However, the presence of amorphous impurity phases cannot be ruled out by the PXRD experiment.

Elemental analysis

The chemical composition of the XRD-pure sample LCP-MW was determined by CHNS, photometry, and AAS analyses. The results are given in Table 1. The measured absolute contents (in wt%) show a deficiency both in Co and P compared to the expected values. This can be attributed to the higher-than-expected amounts of Li and S, which result in a relative decrease of the former elements. The calculated Li : Co : P molar ratio is found to be 1.14(5) : 1.00(1) : 1.00(2). The deviation of the Li value from the theoretical value of 1 : 1 : 1 might be due to some amorphous or trace impurities. CHNS analysis shows that the sample does not contain detectable amounts of carbon that might add to the electrochemical performance, which is confirmed by the absence of any carbon D or G bands in the Raman spectrum (Fig. S7c and d, ESI†). This indicates that the washing step is efficient for the removal of the EG co-solvent or the ascorbic acid additive and their decomposition products. Also no H (*e.g.* from residual water) can be found, but significant amounts of sulfur are detected. Taking the slight excess of about 0.3 wt% Li into account, the S content of 1.5 ± 0.3 wt% can be related to a mixture of $Li_2SO_4 \cdot H_2O$ and Li_2SO_4 impurities. The Li_2SO_4 originates from $Li_2SO_4 \cdot H_2O$, a side product of the synthesis (Scheme 1a, see also Fig. S2, ESI†). The dehydrated form is obtained because of the drying step of the process at 150 °C (dehydration at 130 °C, Scheme 1b).[67,68]

Because Li_2SO_4 has hygroscopic properties,[69] we assume that a mixture of the anhydrous and monohydrate form is present, although the detected hydrogen amounts in the sample were negligible and the IR spectrum does neither show absorption

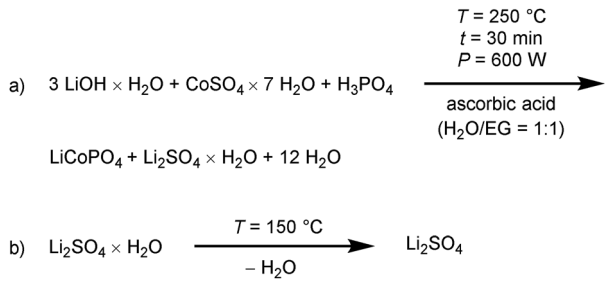

Scheme 1 (a) Reaction scheme of the microwave-assisted solvothermal synthesis, (b) dehydration of the lithium sulfate monohydrate side phase.

Table 1 Elemental analysis (CHNS, AAS, photometry) of the LCP samples LCP-MW and LCP-MW-w in comparison with the theoretical values[a,b,c]

Element	Theor.	(a) LCP-MW	(b) LCP-MW-w
S (wt%)	0	1.5(3)	1.6(3)
Li (wt%)	4.3	4.6(2)	4.5(2)
Co (wt%)	36.6	34.3(5)	34.1(5)
P (wt%)	19.3	18.0(5)	17.7(5)
n(Li) : n(P)	1	1.14(5)	1.13(5)
n(Co) : n(P)	1	1.00(1)	1.01(1)
Li_2SO_4 (wt%)	0	5(1)	6(1)
$LiCoPO_4$ (wt%)	100	94(2)	92(2)

[a] LCP-MW: as-synthesized, LCP-MW-w: after additional extensive washing with ice water to remove solution-accessible Li_2SO_4. [b] The molar ratios are calculated from the experimental results (in wt%) of the CHNS, AAS, and photometric analyses (standard deviations are given in parenthesis). [c] The values for C, H, and N were too low to be measured in all samples (= 0).

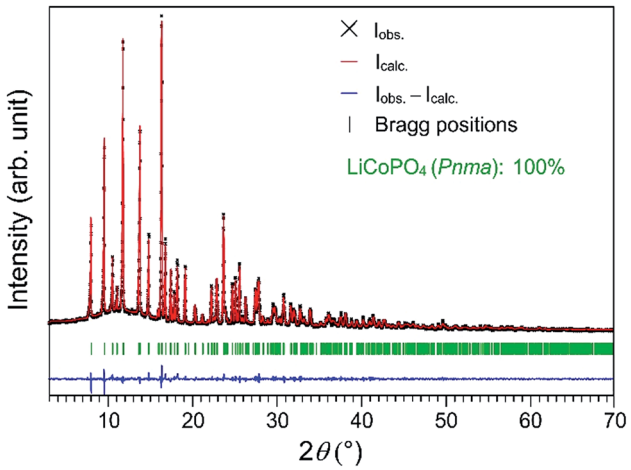

Fig. 2 Rietveld fit of the X-ray powder diffraction data of the as-prepared LCP-MW material obtained from the microwave-assisted solvothermal synthesis.

bands of water nor of lithium sulfate (*cf.* Fig. S7a and b, ESI†). In addition, the estimated 5 ± 1 wt% of lithium sulfate are amorphous and thus not detectable by PXRD in the LCP-MW powder. TGA/DSC and temperature-dependent *in situ* PXRD experiments indicate that the amorphous impurity can be crystallized upon heating (Fig. S4–S6, ESI†).

As equal molar amounts of $LiCoPO_4$ and $Li_2SO_4 \cdot H_2O$ are formed during the reaction according to Scheme 1a, we assume that the biggest portion of the water-soluble lithium sulfate is dissolved in the water component of the binary solvent and further removed by the washing step. In order to completely remove the impurity, we tried to wash the sample extensively with 1 L of ice water, as the solubility of lithium sulfate in water increases with decreasing temperature.[70,71] The S content of the corresponding sample LCP-MW-w remains similar (Table 1), indicating that the impurity cannot be removed by additional washing. We therefore infer that the remaining minor impurity might form inclusions inside the particles rather than being located on their surface, and that >94 ± 2 wt% of the sample are the pure LCP phase. Further experiments with alternative sulfate-free starting materials (*e.g.* chlorides, nitrates) indicate that the Li_2SO_4 impurity cannot be avoided because impure materials or inferior electrochemical performances were observed. Therefore, we consider the sulfate route as the most feasible one, as it also allows the removal of a major portion of the water-soluble side product by washing.

Scanning electron microscopy

Fig. 3 shows the SEM images of the as-prepared sample LCP-MW. The material consists of uniform, well-crystallized and dispersed hexagonal platelets with dimensions of about 400–600 nm × 700–800 nm and thicknesses ranging from about 100 nm to 250 nm. The observed particle size is consistent with the value of the specific surface area (BET) of 5.5 ± 0.5 $m^2\ g^{-1}$. Furthermore, no agglomerates of particles are observed (Fig. 3a and c), indicating that the EG co-solvent helps to prevent agglomeration of the particles without requiring an additional dispersant. Moreover, small pores of 10–20 nm (*cf.* zoomed SEM image, Fig. S9,

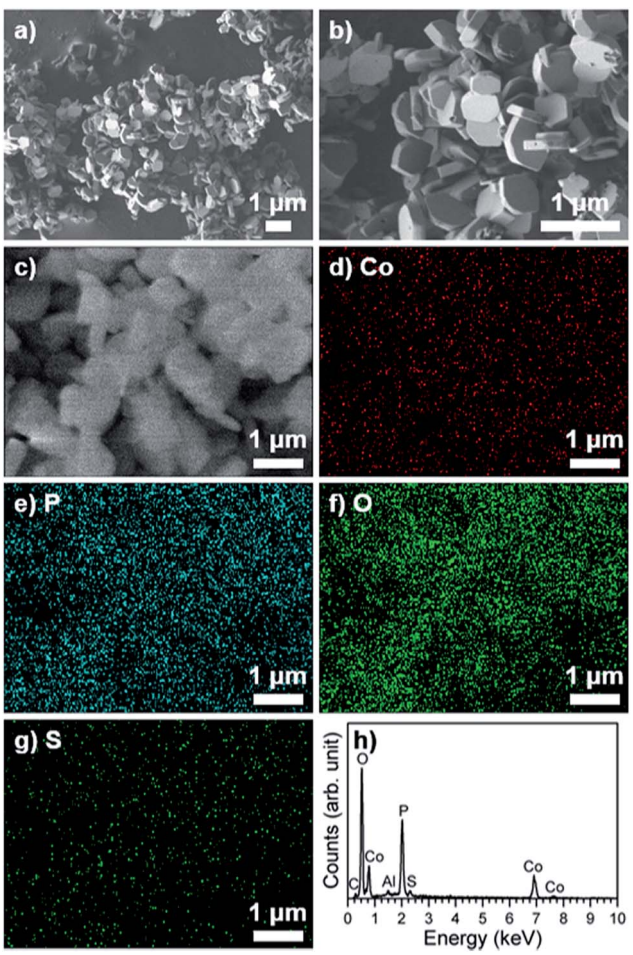

Fig. 3 (a and b) SEM images of LCP-MW recorded at 1 keV (GB mode), (c–g) SEM image and EDS maps for Co, P, O, and S obtained at 15 keV to optimize EDS signals, and (h) representative EDS spectrum. The C and Al signals derive from the carbon tape and the aluminum holder used for the measurement.

ESI,† and TEM images, Fig. 4) in diameter are found on the surface of the particles that can most probably be attributed to the formation mechanism. According to Scheme 1a, $LiCoPO_4$ and Li_2SO_4 are formed in parallel during the reaction and seem to initially form perfect hexagonal composite particles. The highly water soluble Li_2SO_4 is dissolved in solvent as well as in the washing water used after the synthesis. Hence, pores appear on the surface of the particles where the Li_2SO_4 impurity phase was formerly located. The pores, which might be interconnected, destabilize the particles, with some particles showing cracks probably due to mechanical stress during the synthesis produced by stirring and the washing step. As a result, the particle size distribution is slightly inhomogeneous. This explanation was confirmed by further experiments with different amounts of washing water, whereby the extent of fragmentation increased with increasing volumes of water. For instance, the SEM images of the extensively washed sample LCP-MW-w (Fig. S10†) show significantly more fragmented platelets. Therefore, the sample LCP-MW was chosen for further characterization.

Energy dispersive spectroscopic (EDS) analysis under SEM (15 kV; Fig. 3h) delivers a composition of 33 ± 2 wt% Co, 17.4 ± 0.5 wt% P, 48 ± 1 wt% O, and 1.4 ± 0.2 wt% S. These values are in good agreement with the results of the elemental analysis (Table 1). The corresponding Co : P molar ratio is 0.99(6). The elemental distribution was examined using EDS mapping (Fig. 3d–g; please note that the overview image of Fig. 3c suffers from charging effects due to the high accelerating voltage of 15 kV). As expected, all the elements are homogeneously distributed within the sample. It is affirmed that the sulfur shows a regular distribution within the particles, suggesting that the amorphous Li_2SO_4 phase is most likely forming inclusions in the hexagonal platelets and therefore cannot be removed by intensive washing as observed from elemental analysis for the sample LCP-MW-w (Table 1).

The results clearly indicate that the mixed solvent of H_2O and EG significantly influences the morphology of the obtained LCP powder. Whereas the water component promotes the complete dissolution of the reagents and therefore helps to form a more homogeneous reaction mixture, the EG component plays an important role in controlling the particle size and shape. The size-regulating effect can be attributed to the increased viscosity of the binary solvent in comparison to pure water. Hence, the ion diffusion rate is slowed down and therefore prevents the growth of large particles. As a result, comparably narrow particle size distributions are obtained. In addition, the EG components inhibits agglomeration of the primary particles. The polar EG molecules are reported to form long hydrogen-bonding chains, that can trap the cations present in the reaction mixture due to its chelating ability and therefore help the olivine to nucleate and grow into particles with specific morphologies.[54,72] Therefore, EG not only acts as a solvent, but also shows properties of a soft template.[54,73]

Transmission electron microscopy

In order to get a better understanding of the structure and morphology of the material and therefore the formation mechanism and crystal growth, transmission electron microscopy (TEM) in combination with selected area electron diffraction (SAED) experiments was performed. The low resolution image (Fig. 4a) is in agreement with the results of the SEM studies and shows well-defined hexagonal platelets with dimensions of 700–800 nm × 400–600 nm × 100–220 nm. In the SAED study, patterns of several individual crystals were taken to verify that all crystals exhibit identical orientations. In addition to that, diffraction patterns of perpendicular crystal faces were recorded. This approach allows reliable information about the crystal growth orientation as well as the thickness of the platelets. The frontal view of a regular hexagonal platelet (Fig. 4b and c) shows that the particles are highly ordered single crystals that are grown in the *ac* plane, the *c* axis being oriented diagonally along the longest dimension. The pore structure or inclusions within the particles, can be seen in the irregular transmission of the platelet that possesses an unflawed contour. The side view (Fig. 4d–f) reveals that the platelets show the smallest dimension along [010], which is the direction of the lithium diffusion pathways in the olivine crystal structure. Hence, the platelet-like morphology with shorter lithium diffusion pathways enhances the Li diffusion properties. The Fig. 4g–i show a highly fragmented platelet, the hexagonal shape of which is still indicated. Here, the pores have formed an interconnected system, which may be a result of the removal of the water soluble Li_2SO_4 impurity that is formed within the particles. Despite the defective morphology, the single-crystalline particle still shows high crystallinity.

In agreement with previous reports,[73,74] the TEM studies indicate that the EG co-solvent specifically adsorbs on the

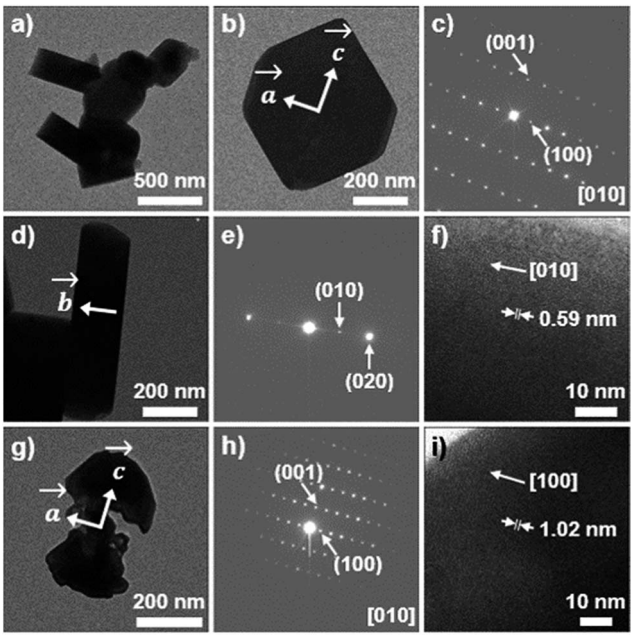

Fig. 4 TEM images, corresponding SAED (selected area electron diffraction) patterns, and HRTEM images of LCP-MW: (a) overview image, (b and c) frontal view of a hexagonal platelet, (d–f) side view of a platelet, and (g–i) particle with a porous structure as a result of the removal of the water soluble Li_2SO_4 impurity.

(010) crystal face, therefore dramatically decreasing its surface energy. As a result, the growth along [010] is inhibited. In addition, the nanoplatelets grow preferentially along the [001] direction of the (010) plane due to the higher surface energy of the (001) than that of the (100) plane,[72] promoting the formation of unique hexagonal platelets with reduced dimensions along *b*. A more thorough formation mechanism cannot be derived at this point and will have to be further examined. However, the observation of hexagonal shapes with exposed (010) faces is consistent with calculations of the surface energies of LFP by Fisher and Islam,[75] who suggested the favorable growth morphology under hydrothermal conditions to be an hexagonal prism terminated by (010), (100), and (101) faces.

Soft X-ray spectroscopy

The normalized soft XAS Co $L_{2,3}$-edge spectra for the sample LCP-MW are shown along with two reference compounds (CoO and Co_3O_4 powder) in Fig. 5. Whereas K-edge spectra have been obtained in various studies,[76–78] to the best of our knowledge, this is the first time the Co L-edge data of $LiCoPO_4$ are presented. The XAS was collected in the Auger electron yield (AEY), total electron yield (TEY), and fluorescence yield (FY) modes, corresponding to probing depths of 1–2 nm, 2–5 nm and 50 nm, respectively.[62] The absorption peaks of the $L_{2,3}$-edge XAS are sensitive to the oxidation state, spin state, and the chemical environment in the crystal.[79]

We note that the main peaks in the spectra line up with the CoO reference spectra. A comparison with Co $L_{2,3}$-edge spectra reported for other Co(II) and Co(III) compounds in various symmetries, as well as the lowest energy peak at 776.4 eV give strong evidence for octahedral Co^{2+} as expected, showing a similar crystal field strength as in CoO.[63,79–81] The well-defined multiplet structure indicates a highly ordered crystal structure and a low degree of covalence in the CoO_6 octahedra,[63] which is consistent with the sharp peaks observed in the PXRD (Fig. 2) and in general agreement with earlier findings for LFP through Fe $L_{2,3}$-edge spectra.[82,83] The oxidation state is consistently +II for all detection modes and hence, indicates that the sample is homogeneous from the top surfaces to volumes deep in the bulk. The absence of a shoulder at the characteristic peak energy for Co^{3+} (779.4 eV) shows that there are no significant amounts of Co^{3+} impurities, also not on the surface, which might reduce the electrochemical activity. The small amount of the ascorbic acid reductant used in the synthesis therefore seems to be sufficient to prevent oxidation of Co^{2+} in solution. The EG solvent can also act as a weak reducing agent.[73]

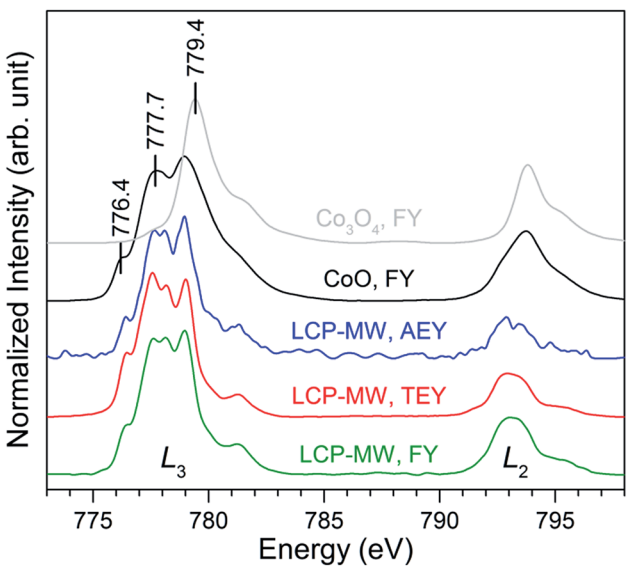

Fig. 5 Normalized soft XAS Co $L_{2,3}$-edge spectra of LCP-MW recorded in the AEY (blue), TEY (red), and FY (green) modes in comparison to the FY modes of the reference compounds CoO (black) and Co_3O_4 (grey). The energies corresponding to O_h Co^{2+} (776.4 eV), Co^{2+} (777.7 eV), and Co^{3+} (779.4 eV) are indicated.

Electrochemical characterization

The electrochemical performances of the LCP synthesized by MWST synthesis (LCP-MW) are presented in Fig. 6. In order to gauge the obtained data, a comparison with a LCP material with spherical nanoparticles (diameter ~50–60 nm, BET area ~25 $m^2\ g^{-1}$) obtained by solid-state synthesis (LCP-SS) as described in our previous work[84] was added. The rate capability of the LCP-MW electrode was investigated (Fig. 6a). The corresponding galvanostatic curves of the 3rd cycle at 0.1 C and 0.5 C are shown in Fig. 6b. During the 1st cycle at 0.1 C, LCP-MW reaches an initial discharge capacity of 137 mA h g^{-1} whereas only 125 mA h g^{-1} is obtained for LCP-SS. The charge curve (Fig. 6b) is characterized by two potential plateaus at 4.75 V and 4.86 V for LCP-MW. For LCP-SS, the plateaus are slightly at higher potential values with 4.8 V and 4.9 V. Both potential windows are in agreement with earlier reports for LCP.[85,86] The discharge curves also present two potential plateaus which are shifted to lower potential for LCP-SS. The corresponding gravimetric energy densities of the materials based on the mean values of the potential of ~4.8 V and ~4.75 V are 658 W h kg^{-1} for LCP-MW and 594 W h kg^{-1} for LCP-SS, respectively. For the first six cycles corresponding to rates of 0.1 C and 0.2 C, the difference in specific capacity between the samples was similar, with values of 120 mA h g^{-1} and 108 mA h g^{-1} found for LCP-MW and LCP-SS at the end of cycle 6, respectively. At these low C rates, the coulombic efficiency, which improved upon cycling, was higher for LCP-MW than for LCP-SS, at 96.7% and 94.5%, respectively, after six cycles. The low coulombic efficiency values in the first cycle are caused by the decomposition of the electrolyte during the charge at high potential.[87] The better efficiency obtained for LCP-MW can be explained by its lower surface area (~6 $m^2\ g^{-1}$ compared to ~25 $m^2\ g^{-1}$ (ref. 84) for LCP-SS), as parasitic currents from electrolyte oxidation at high potentials would be estimated to be proportional to the BET surface area. The about fourfold lower BET surface area of LCP-MW should thus lead to the observed substantially improved coulombic efficiency. From 0.5 C to 2 C, the difference in specific capacity between LCP-MW and LCP-SS increased. At the end of the cycling procedure at a 2 C rate, a specific capacity

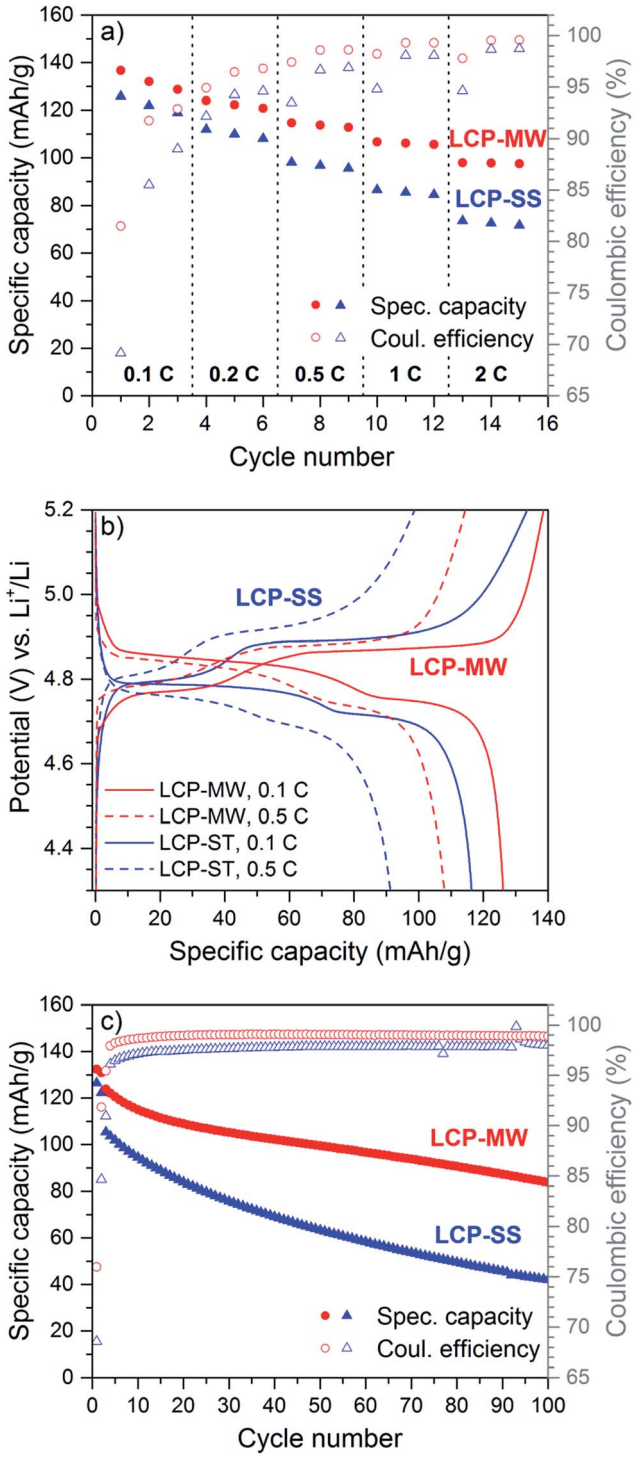

Fig. 6 (a) Specific capacity *vs.* C rate and coulombic efficiency obtained in each cycle for LCP-MW in comparison to LCP-SS, (b) galvanostatic curves for the 3rd cycle at 0.1 C and at 0.5 C, (c) comparison of the electrochemical stabilities of LCP-MW and LCP-SS at 0.5 C after the first two cycles at 0.067 C.

of 98 mA h g^{-1} was reached for LCP-MW, whereas 71 mA h g^{-1} was obtained for LCP-SS. LCP-MW is able to sustain higher currents than LCP-SS, probably due to its unique platelet-like shape with shorter lithium diffusion paths as discussed earlier. This hypothesis is also supported by the lower charge/discharge polarization of the LCP-MW compared to LCP-SS (Fig. 6b), despite of its fourfold lower BET area. Additionally, some tests at lower current (0.067 C) were done for LCP-SS but no improvement in the specific capacity was obtained.

The electrochemical stability of both LCP materials was investigated at 0.5 C rate after two formation cycles at 0.067 C (Fig. 6c). The very low coulombic efficiencies in the first two cycles are due to the very low C rates, at which parasitic currents from electrolyte oxidation more strongly affect the coulombic efficiency. For the first cycle at 0.5 C, the specific capacity reaches 123 mA h g^{-1} for LCP-MW and only 106 mA h g^{-1} for LCP-SS. After 100 cycles, a specific capacity of 84 mA h g^{-1} is obtained for LCP-MW whereas only half of this value is found for LCP-SS. A coulombic efficiency of 98.9% is quickly reached for LCP-MW, which is higher than the one of LCP-SS. The better electrochemical behavior in the 1st cycle combined with a higher coulombic efficiency are probably responsible of the higher stability observed for LCP-MW.

In order to elucidate whether the amorphous lithium sulfate impurity (~5 wt%) affects the electrochemical properties, samples with similar particle size and shape but varying amounts of Li_2SO_4 were synthesized by the MWST process. As all samples show comparable electrochemical performance within standard deviations (Fig. S11 and S12, ESI†), the results indicate that the impurity does not influence the electrochemical behavior, and that it is electrochemically inactive.

To sum up, we have demonstrated that the LCP produced by MWST synthesis outperforms a compound synthesized by a conventional solid-state reaction, which is the standard method for synthesizing $LiCoPO_4$ in the bulk scale.

Comparison with the literature

Research in the field of hydro- and solvothermal synthesis of LCP has been ongoing since 2005.[36] The electrochemical properties of materials synthesized by the hydrothermal technique were first reported in 2009 and a capacity of only 15 mA h g^{-1} reached.[38] An improvement of the performance has been exclusively realized by additional post-calcinations at temperatures as high as 900 °C and/or coating with conductive carbon to give $LiCoPO_4$/C, the only exception being the MWST synthesis (Fig. 7). Hence, it is important to note that the capacities of uncoated $LiCoPO_4$, which reflects the intrinsic capacity of the material, and $LiCoPO_4$/C are comparable to only a limited degree. In fact, by introducing carbon coatings, the energy density is decreased. Hence, the carbon content has to be kept a relatively low levels, even if there is an apparent improvement in rate capability.[88] In addition, also the cell design, charging protocol (C rate, potential window, CV step, *etc.*) as well as post-synthetic treatments influence the electrochemical performance.

In comparison to the state of the art in conventional as well as microwave-assisted hydro- and solvothermal synthesis of pure LCP-type materials, reflecting the intrinsic material properties, our material LCP-MW in fact delivers the best

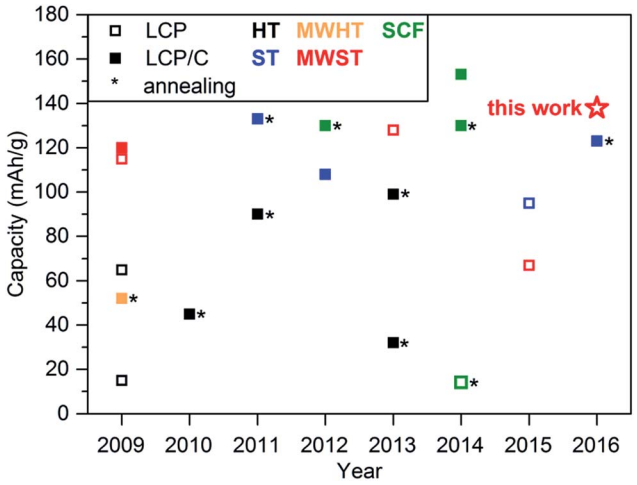

Fig. 7 Comparison of the initial discharge capacities obtained for $LiCoPO_4$ and carbon-coated $LiCoPO_4$/C materials synthesized *via* hydrothermal (HT),[38–40,42] solvothermal (ST),[42–44,53,90] microwave-assisted hydro- (MWHT)[47] and solvothermal (MWST),[48,50,51] and supercritical fluid (SCF)[28,29,55,78] procedures as reported between 2009 and 2016. Asterisks mark materials that underwent additional post-heat treatments at high temperatures. The star represents the capacity reached in this work using a MWST approach, which is the best reported for an untreated LCP-type material to date.

electrochemical performance to date. In comparison to materials that underwent further treatments such as post-annealing or conductive coatings, our as-prepared material also delivers a state-of-the-art performance, which is remarkable. Moreover, our material was tested in a regular setup using standard electrolytes (EC/DMC) and medium loadings (4–5 mg cm^{-2}). Additional tests with high loadings up to 12 mg cm^{-2} were done and present reasonable specific capacity (Fig. S13, ESI†). Further improvements can be expected upon optimization of the electrolyte (*e.g.*, using ionic liquids or additives such as trimethylboroxine[84,89]) and the electrode formulation.[13] In addition, the microwave method allows a considerable reduction of the production costs as it requires only moderate temperatures and produces highly crystalline materials in one step without further treatment. Once suitable electrolytes for high-voltage cathodes are available, materials like LCP might be sustainable candidates for future Li-ion battery applications.

Conclusions

High-performance $LiCoPO_4$ particles with uniform hexagonal platelet-like morphologies have been synthesized by a facile and rapid microwave-assisted solvothermal approach at moderate temperatures (250 °C) using a water/ethylene glycol (EG) (1 : 1) mixed solvent. Unlike conventional hydrothermal or solvothermal techniques, the process does not involve any additional post heat treatment or carbon coating. PXRD patterns indicate the direct formation of highly crystalline, olivine-type $LiCoPO_4$ from the microwave synthesis. SEM and TEM/SAED studies reveal that the hexagonal platelets feature dimensions of 800 nm × 300–400 nm in the (010) plane and a thickness of 200–300 nm along [010]. The results indicate that EG plays an important role in the formation of the $LiCoPO_4$ nanoplatelets by effectively regulating the particle size and morphology as well as tuning the crystal orientation.

The nanoplatelets exhibit excellent electrochemical properties, including a high initial discharge capacity of 137 mA h g^{-1} at 0.1 C, 114 mA h g^{-1} at 0.5 C, and 97 mA h g^{-1} at 2 C, high coulombic efficiency, and excellent rate capability. Moreover, the material displays a remarkable stable capacity retention of 68% after 100 cycles at 0.5 C. These attractive electrochemical features can be attributed to the unique submicron scale platelet-like morphology with shortened lithium-ion diffusion pathways along the *b* direction of the crystal structure. Never-theless, a possible effect of the amorphous, sulfur-containing Li_2SO_4/$Li_2SO_4 \cdot H_2O$ impurity (<5 wt%), which was identified by means of elemental analysis, EDS, and temperature-dependent X-ray powder diffraction experiments, on the electrochemical features will have to be addressed in further experiments.

To conclude, the present work provides an efficient and simple approach towards high-performance olivine-type cathode materials with designed morphology. Moreover, it clarifies the relationship between the synthesis method, material microstructure and electrochemical properties, which has hitherto barely been touched upon in the literature but is crucial for developments in the field. The short reaction time as well as the fact that the one-step microwave process does not involve any post-treatments (*e.g.* annealing, coating, ball milling) offer the potential to lower the manufacturing costs of cathode materials with significant energy savings in comparison to other synthesis techniques.

Abbreviations

AEY	Auger electron yield
AAS	Atomic absorption spectroscopy
DMC	Dimethyl carbonate
EC	Ethylene carbonate
EDS	Energy-dispersive X-ray spectroscopy
EG	Ethylene glycol
FY	Fluorescence yield
GB	Gentle beam
HT	Hydrothermal
LCP	Lithium cobalt phosphate
LFP	Lithium iron phosphate
LMP	Lithium manganese phosphate
LNP	Lithium nickel phosphate
MWST	Microwave-assisted solvothermal
NMP	*N*-Methyl-2-pyrrolidone
PTFE	Poly(tetrafluoroethylene)
PVDF	Polyvinylidene difluoride
PXRD	Powder X-ray diffraction
SAED	Selected area electron diffraction
SFC	Supercritical fluid
SEM	Scanning electron microscope
SS	Solid-state
ST	Solvothermal

TEM	Transmission electron microscopy
TEY	Total electron yield
XAS	X-ray absorption spectroscopy

Acknowledgements

The authors would like to thank the BMW AG, the state of Bavaria, and the TUM for financial support and funding. The soft XAS experiments were carried out at the Stanford Synchrotron Radiation Lightsource, a Directorate of SLAC National Accelerator Laboratory and an Office of Science User Facility operated for the US Department of Energy Office of Science by Stanford University (contract no. DE-AC02-76SF00515). Furthermore, we thank Prof. J. Mink for Raman, K. Rodewald for SEM, and M. Hanzlik for TEM measurements. We also thank U. Ammari of the microanalytical laboratory of the TUM for elemental analyses. The help of Y. Li with the temperature-dependent PXRD measurements is gratefully acknowledged. J. Ludwig is further grateful to the Fonds der Chemischen Industrie for her fellowship.

References

1 A. K. Padhi, K. S. Nanjundaswamy and J. B. Goodenough, *J. Electrochem. Soc.*, 1997, **144**, 1188–1194.
2 J. M. Tarascon and M. Armand, *Nature*, 2001, **414**, 359–367.
3 S. Okada, S. Sawa, M. Egashira, J. Yamaki, M. Tabuchi, H. Kageyama, T. Konishi and A. Yoshino, *J. Power Sources*, 2001, **97–98**, 430–432.
4 M. Piana, M. Arrabito, S. Bodoardo, A. D'Epifanio, D. Satolli, F. Croce and B. Scrosati, *Ionics*, 2002, **8**, 17–26.
5 S.-Y. Chung, J. T. Bloking and Y.-M. Chiang, *Nat. Mater.*, 2002, **1**, 123–128.
6 B. L. Ellis, K. T. Lee and L. F. Nazar, *Chem. Mater.*, 2010, **22**, 691–714.
7 K. Zaghib, A. Guerfi, P. Hovington, A. Vijh, M. Trudeau, A. Mauger, J. B. Goodenough and C. M. Julien, *J. Power Sources*, 2013, **232**, 357–369.
8 W.-J. Zhang, *J. Power Sources*, 2011, **196**, 2962–2970.
9 B. Kang and G. Ceder, *Nature*, 2009, **458**, 190–193.
10 Y. Wang, P. He and H. Zhou, *Energy Environ. Sci.*, 2011, **4**, 805–817.
11 A. Yamada, M. Hosoya, S.-C. Chung, Y. Kudo, K. Hinokuma, K.-Y. Liu and Y. Nishi, *J. Power Sources*, 2003, **119–121**, 232–238.
12 C. M. Julien and A. Mauger, *Ionics*, 2013, **19**, 951–988.
13 M. Hu, X. Pang and Z. Zhou, *J. Power Sources*, 2013, **237**, 229–242.
14 K. Amine, H. Yasuda and M. Yamachi, *Electrochem. Solid-State Lett.*, 2000, **3**, 178–179.
15 J. Wolfenstine and J. Allen, *J. Power Sources*, 2005, **142**, 389–390.
16 L. Dimesso, C. Spanheimer and W. Jaegermann, *Solid State Sci.*, 2012, **14**, 1372–1377.
17 J. Wolfenstine, *J. Power Sources*, 2006, **158**, 1431–1435.
18 J. L. Allen, T. Thompson, J. Sakamoto, C. R. Becker, T. R. Jow and J. Wolfenstine, *J. Power Sources*, 2014, **254**, 204–208.
19 M. Prabu, S. Selvasekarapandian, A. R. Kulkarni, S. Karthikeyan, G. Hirankumar and C. Sanjeeviraja, *Solid State Sci.*, 2011, **13**, 1714–1718.
20 K. Hayashi, Y. Nemoto, S.-I. Tobishima and J.-I. Yamaki, *Electrochim. Acta*, 1999, **44**, 2337–2344.
21 M. Egashira, H. Takahashi, S. Okada and J.-I. Yamaki, *J. Power Sources*, 2001, **92**, 267–271.
22 C. A. J. Fisher, P. V. M. Hart and M. S. Islam, *Chem. Mater.*, 2008, **20**, 5907–5915.
23 J. L. Allen, T. R. Jow and J. Wolfenstine, *J. Power Sources*, 2011, **196**, 8656–8661.
24 J. Wolfenstine, J. Read and J. L. Allen, *J. Power Sources*, 2007, **163**, 1070–1073.
25 P. R. Kumar, V. Madhusudhanrao, B. Nageswararao, M. Venkateswarlu and N. Satyanarayana, *J. Solid State Electrochem.*, 2016, **20**, 1855–1863.
26 J. Liu, T. E. Conry, X. Song, L. Yang, M. M. Doeff and T. J. Richardson, *J. Mater. Chem.*, 2011, **21**, 9984–9987.
27 S. Brutti, P. Reale, E. Piciollo, V. Gentili, P. G. Bruce, B. Scrosati and S. Panero, *Prepr. Symp. – Am. Chem. Soc., Div. Fuel Chem.*, 2012, **57**, 737–739.
28 M. K. Devaraju, D. Rangappa and I. Honma, *Electrochim. Acta*, 2012, **85**, 548–553.
29 X. Rui, X. Zhao, Z. Lu, H. Tan, D. Sim, H. H. Hng, R. Yazami, T. M. Lim and Q. Yan, *ACS Nano*, 2013, **7**, 5637–5646.
30 M.-S. Park, J. Kim, K. J. Kim, J.-W. Lee, J. H. Kim and Y. Yamauchi, *Phys. Chem. Chem. Phys.*, 2015, **17**, 30963–30977.
31 D. Morgan, A. Van der Ven and G. Ceder, *Electrochem. Solid-State Lett.*, 2003, **7**, A30–A32.
32 S.-I. Nishimura, G. Kobayashi, K. Ohoyama, R. Kanno, M. Yashima and A. Yamada, *Nat. Mater.*, 2008, **7**, 707–711.
33 N. N. Bramnik, K. G. Bramnik, T. Buhrmester, C. Baehtz, H. Ehrenberg and H. Fuess, *J. Solid State Electrochem.*, 2004, **8**, 558–564.
34 J. Wolfenstine, U. Lee, B. Poese and J. L. Allen, *J. Power Sources*, 2005, **144**, 226–230.
35 M. E. Rabanal, M. C. Gutierrez, F. Garcia-Alvarado, E. C. Gonzalo and M. E. Arroyo-de Dompablo, *J. Power Sources*, 2006, **160**, 523–528.
36 X. Huang, J. Ma, P. Wu, Y. Hu, J. Dai, Z. Zhu, H. Chen and H. Wang, *Mater. Lett.*, 2005, **59**, 578–582.
37 J. Chen, S. Wang and M. S. Whittingham, *J. Power Sources*, 2007, **174**, 442–448.
38 Y. Zhao, S. Wang, C. Zhao and D. Xia, *Rare Met.*, 2009, **28**, 117–121.
39 M. Kotobuki, Y. Mizuno, H. Munakata and K. Kanamura, *Phosphorus Res. Bull.*, 2010, **24**, 12–15.
40 M. Kotobuki, *Int. J. Energy Environ. Eng.*, 2013, **4**, 25–27.
41 J. Su, B.-Q. Wei, J.-P. Rong, W.-Y. Yin, Z.-X. Ye, X.-Q. Tian, L. Ren, M.-H. Cao and C.-W. Hu, *J. Solid State Chem.*, 2011, **184**, 2909–2919.
42 F. Wang, J. Yang, Y. Nuli and J. Wang, *J. Power Sources*, 2011, **196**, 4806–4810.
43 M. Li, *Ionics*, 2012, **18**, 507–512.

44 S. Brutti, J. Manzi, A. De Bonis, D. Di Lecce, F. Vitucci, A. Paolone, F. Trequattrini and S. Panero, *Mater. Lett.*, 2015, **145**, 324–327.
45 M. K. Devaraju and I. Honma, *Adv. Energy Mater.*, 2012, **2**, 284–297.
46 J. A. Gerbec, D. Magana, A. Washington and G. F. Strouse, *J. Am. Chem. Soc.*, 2005, **127**, 15791–15800.
47 A. V. Murugan, T. Muraliganth and A. Manthiram, *J. Electrochem. Soc.*, 2009, **156**, A79–A83.
48 A. V. Murugan, T. Muraliganth, P. J. Ferreira and A. Manthiram, *Inorg. Chem.*, 2009, **48**, 946–952.
49 C. Neef, C. Jaehne and R. Klingeler, *Lect. Notes Impedance Spectrosc.*, 2012, **3**, 91–93.
50 R. E. Rogers, G. M. Clarke, O. N. Matthew, M. J. Ganter, R. A. DiLeo, J. W. Staub, M. W. Forney and B. J. Landi, *J. Appl. Electrochem.*, 2013, **43**, 271–278.
51 K. J. Kreder, G. Assat and A. Manthiram, *Chem. Mater.*, 2015, **27**, 5543–5549.
52 I. Bilecka and M. Niederberger, *Nanoscale*, 2010, **2**, 1358–1374.
53 B. Wu, H. Xu, D. Mu, L. Shi, B. Jiang, L. Gai, L. Wang, Q. Liu, L. Ben and F. Wu, *J. Power Sources*, 2016, **304**, 181–188.
54 M. Wu, Z. H. Wang, L. X. Yuan, W. X. Zhang, X. L. Hu and Y. H. Huang, *Chin. Sci. Bull.*, 2012, **57**, 4170–4175.
55 Q. D. Truong, M. K. Devaraju, Y. Ganbe, T. Tomai and I. Honma, *Sci. Rep.*, 2014, **4**, 3975.
56 H. Liang and L. Zhang, *Russ. J. Electrochem.*, 2014, **50**, 297–300.
57 V. Petricek, M. Dusek and L. Palatinus, *Z. Kristallogr. - Cryst. Mater.*, 2014, **229**, 345–352.
58 L. W. Finger, D. E. Cox and A. P. Jephcoat, *J. Appl. Crystallogr.*, 1994, **27**, 892–900.
59 D. T. Cromer and D. A. Liberman, *Acta Crystallogr., Sect. A: Cryst. Phys., Diffr., Theor. Gen. Crystallogr.*, 1981, **A37**, 267–268.
60 J. F. Berar and P. Lelann, *J. Appl. Crystallogr.*, 1991, **24**, 1–5.
61 D. C. Palmer, *CrystalMaker 2.5.5*, CrystalMaker Software Ltd, Begbroke, Oxfordshire, England, 2012.
62 F. Lin, D. Nordlund, I. M. Markus, T.-C. Weng, H. L. Xin and M. M. Doeff, *Energy Environ. Sci.*, 2014, **7**, 3077–3085.
63 A. M. Hibberd, H. Q. Doan, E. N. Glass, F. M. F. de Groot, C. L. Hill and T. Cuk, *J. Phys. Chem. C*, 2015, **119**, 4173–4179.
64 V. Koleva, E. Zhecheva and R. Stoyanova, *Eur. J. Inorg. Chem.*, 2010, 4091–4099.
65 M. K. Devaraju, Q. D. Truong, H. Hyodo, T. Tomai and I. Honma, *Inorganics*, 2014, **2**, 233–247.
66 J. Chen, M. J. Vacchio, S. Wang, N. Chernova, P. Y. Zavalij and M. S. Whittingham, *Solid State Ionics*, 2008, **178**, 1676–1693.
67 H. Tanaka, *Thermochim. Acta*, 1982, **52**, 195–199.
68 F. Valdivieso, V. Bouineau, M. Pijolat and M. Soustelle, *Solid State Ionics*, 1997, **101–103**, 1299–1303.
69 R. Weintraub, A. Apelblat and A. Tamir, *Anal. Chim. Acta*, 1984, **166**, 325–327.
70 J. A. N. Friend, *J. Chem. Soc.*, 1929, 2330–2333.
71 W. F. Linke and A. Seidell, *Solubilities of In-organic and Metal Organic Compounds*, Am. Chem. Soc., 4th edn, 1966, vol. 2.
72 J. Song, L. Wang, G. Shao, M. Shi, Z. Ma, G. Wang, W. Song, S. Liu and C. Wang, *Phys. Chem. Chem. Phys.*, 2014, **16**, 7728–7733.
73 S. Kuppan, P. Balaya, M. V. Reddy, B. V. R. Chowdari and J. J. Vittal, *Energy Environ. Sci.*, 2010, **3**, 457–464.
74 X. Qin, J. Wang, J. Xie, F. Li, L. Wen and X. Wang, *Phys. Chem. Chem. Phys.*, 2012, **14**, 2669–2677.
75 C. A. J. Fisher and M. S. Islam, *J. Mater. Chem.*, 2008, **18**, 1209–1215.
76 M. Nakayama, S. Goto, Y. Uchimoto, M. Wakihara, Y. Kitajima, T. Miyanaga and I. Watanabe, *J. Phys. Chem. B*, 2005, **109**, 11197–11203.
77 J. L. Shui, Y. Yu, X. F. Yang and C. H. Chen, *Electrochem. Commun.*, 2006, **8**, 1087–1091.
78 M. Kaus, I. Issac, R. Heinzmann, S. Doyle, S. Mangold, H. Hahn, V. S. K. Chakravadhanula, C. Kuebel, H. Ehrenberg and S. Indris, *J. Phys. Chem. C*, 2014, **118**, 17279–17290.
79 F. M. F. de Groot, M. Abbate, J. van Elp, G. A. Sawatzky, Y. J. Ma, C. T. Chen and F. Sette, *J. Phys.: Condens. Matter*, 1993, **5**, 2277–2288.
80 M. M. van Schooneveld, R. Kurian, A. Juhin, K. Zhou, J. Schlappa, V. N. Strocov, T. Schmitt and F. M. F. de Groot, *J. Phys. Chem. C*, 2012, **116**, 15218–15230.
81 M. Ghiasi, M. U. Delgado-Jaime, A. Malekzadeh, R.-P. Wang, P. S. Miedema, M. Beye and F. M. F. de Groot, *J. Phys. Chem. C*, 2016, **120**, 8167–8174.
82 A. Augustsson, G. V. Zhuang, S. M. Butorin, J. M. Osorio-Guillen, C. L. Dong, R. Ahuja, C. L. Chang, P. N. Ross, J. Nordgren and J. H. Guo, *J. Chem. Phys.*, 2005, **123**, 184717.
83 X.-J. Wang, C. Jaye, K.-W. Nam, B. Zhang, H.-Y. Chen, J. Bai, H. Li, X. Huang, D. A. Fischer and X.-Q. Yang, *J. Mater. Chem.*, 2011, **21**, 11406–11411.
84 A. Freiberg, M. Metzger, D. Haering, S. Bretzke, S. Puravankara, T. Nilges, C. Stinner, C. Marino and H. A. Gasteiger, *J. Electrochem. Soc.*, 2014, **161**, A2255–A2261.
85 N. N. Bramnik, K. Nikolowski, C. Baehtz, K. G. Bramnik and H. Ehrenberg, *Chem. Mater.*, 2007, **19**, 908–915.
86 H. Ehrenberg, N. N. Bramnik, A. Senyshyn and H. Fuess, *Solid State Sci.*, 2009, **11**, 18–23.
87 N. N. Bramnik, K. Nikolowski, D. M. Trots and H. Ehrenberg, *Electrochem. Solid-State Lett.*, 2008, **11**, A89–A93.
88 Y. Hong, Z. Tang, S. Wang, W. Quan and Z. Zhang, *J. Mater. Chem. A*, 2015, **3**, 10267–10274.
89 R. Sharabi, E. Markevich, K. Fridman, G. Gershinsky, G. Salitra, D. Aurbach, G. Semrau, M. A. Schmidt, N. Schall and C. Bruenig, *Electrochem. Commun.*, 2013, **28**, 20–23.
90 J. Manzi, M. Curcio and S. Brutti, *Nanomaterials*, 2015, **5**, 2212–2230.

